A model of ocular ambient irradiance at any head orientation

Marro, Michele; Moccozet, Laurent; Vernez, David

How to cite

MARRO, Michele, MOCCOZET, Laurent, VERNEZ, David. A model of ocular ambient irradiance at any head orientation. In: Computers in biology and medicine, 2024, vol. 179, p. 108903. doi: 10.1016/j.compbiomed.2024.108903

This publication URL: https://archive-ouverte.unige.ch/unige:179076
Publication DOI: 10.1016/j.compbiomed.2024.108903

Computers in Biology and Medicine 179 (2024) 108903

Contents lists available at ScienceDirect

Computers in Biology and Medicine

journal homepage: www.elsevier.com/locate/compbiomed

A model of ocular ambient irradiance at any head orientation

Michele Marro [a,*], Laurent Moccozet [a], David Vernez [b]

[a] University of Geneva, Centre Universitaire d'informatique, Battelle, Batiment A, 7 Route de Drize 1227 Carouge (CH), Switzerland
[b] University of Lausanne, Center for Public Health and Primary Care Medicine (Unisanté), 44 Rue du Bugnon 1011 Lausanne (CH), Switzerland

ARTICLE INFO

Keywords:
Modeling
Eye
Ocular
Exposure
Irradiance
Prevention
Health

ABSTRACT

Exposure to ambient ultraviolet radiation is associated with various ocular pathologies. Estimating the irradiance received by the eyes is therefore essential from a preventive perspective and to study the relationship between light exposure and eye diseases. However, measuring ambient irradiance on the ocular surface is challenging. Current methods are either approximations or rely on simplified setups. Additionally, factors like head rotation further complicate measurements for prolonged exposures. This study proposes a novel numerical approach to address this issue by developing an analytical model for calculating irradiance received by the eye and surrounding ocular area. The model takes into account local ambient irradiance, sun position, and head orientation. It offers a versatile and cost-effective means of calculating ocular irradiance, adaptable to diverse scenarios, and serves both as a predictive tool and as a way to compute correction factors, such as the fraction of diffuse irradiance received by the eyes. Furthermore, it can be tailored for prolonged durations, facilitating the calculation of radiant dose obtained during extended exposures.

1. Introduction

Exposure to ultraviolet radiation (UVR) is a leading cause of ocular pathologies [1,2]. Cataract, characterized by opacity of the eye lens, stands among the most prevalent ocular pathologies worldwide [3] and constitutes a significant cause of blindness [4]. UVR can also induce cutaneous pathologies in the periocular region, such as squamous cell carcinoma (SCC) and basal cell carcinoma (BCC) of the eyelids [5]. Pterygium, manifesting as an abnormal growth of the conjunctiva on the eye's surface, has been associated with UVR exposure [6]. Although the pathogenesis remains unknown, its incidence has been correlated with geographical latitude, underscoring the significance of ambient UVR [7]. Recent studies have linked the onset of myopia to a relative decrease in ocular exposure to UV and, more broadly, to daylight in childhood [8].

The sun is the primary source of UVR. On the earth's surface, this wavelength range (including UVA and UVB) constitutes, on average, 9% of the entire electromagnetic spectrum to which we are exposed [9]. However, in terms of energy, the contribution of UVR is greater compared to longer wavelength ranges. [10].

The intensity of ambient UVR is influenced by various factors, including weather conditions and geographical location [11]. Ambient UVR received by the eye during a period of exposure depends on personal activities and time spent outdoors, making the estimation of ocular irradiance challenging [12,13]. Estimating cular exposure is further complicated by the continuous changes in the exposed surface area due to eyelid movements and blinking [14], as well as the rotation of the eye, which affects the total received dose [15].

Various methods have been used to study diurnal and seasonal variations in ocular irradiance, such as using manikins equipped with light sensors [16]. As an example, this approach has specifically provided insights into the inadequacy of the UV index [17]. Given the inherent challenges in directly measuring ocular irradiance, common approaches involve using light sensors placed vertically near the eye to approximate real data, enabling estimations for relatively long exposure periods [18,19]. Due to their compact size and minimal disruption to daily activitie, wearable sensors are also widely utilized for measuring personal exposures [20]; unfortunately, they do not allow for the specific estimation of ocular irradiance.

Contact lenses sensitive to UVR have been used to measure ocular irradiance at the corneal level, although they have significant limitations regarding the duration of measurement [21]. Despite this, they are actively utilized in radiotherapy sessions to quantify the dose of ionizing radiation received [22].

Quantifying ocular exposure to ambient UVR is of paramount importance for studying the exposure-disease relationship and preventing pathologies. However, the measurement methods are limited, and there

* Corresponding author.
E-mail addresses: michele.marro@unige.ch (M. Marro), laurent.moccozet@unige.ch (L. Moccozet), david.vernez@unisante.ch (D. Vernez).

https://doi.org/10.1016/j.compbiomed.2024.108903
Received 18 October 2023; Received in revised form 6 June 2024; Accepted 14 July 2024
Available online 26 July 2024

is no unique method that can be applied universally to the various conditions that may be encountered [16].

The urgent need for a reliable method of estimating ocular irradiance is underscored by the anticipated increase in UVR intensity due to stratospheric ozone depletion, potentially heightening the risk of ocular diseases associated with UVR exposure [23,24].

This study introduces a novel method for the rapid and direct calculation of ocular irradiance in various scenarios. The approach is entirely numerical and leverages the capabilities of a validated numerical model to calculate specific reference data that would be challenging to obtain using conventional methods.

The model is designed to be compatible with the set of variables typically obtained from ambient irradiance measurements or generated by a radiative transfer model. Measuring (or simulating) ambient irradiance poses fewer challenges than measuring the irradiance received by the eyes. Furthermore, the model developed in this study allows for the determination of the conversion factor between ambient irradiance and ocular irradiance.

This versatile and cost-effective calculation method facilitates the determination of the ambient irradiance received by the ocular area, taking into account the complex interaction of head anatomy. This model can be used as a direct method to extract the fraction of ambient irradiance received by the eye in various scenarios. Similarly, it can be iteratively implemented to calculate and predict ocular irradiance during an exposure period in which ambient parameters and head orientation continuously vary.

This article is divided into 4 main sections. In Section 2 (Method), we describe the strategy adopted to derive the model, the definitions, the reference systems in use, and the regression models. In Section 3 (Results), we present the results of the fits and the statistical analyses. In Section 4 (Discussion), we examine the results, applications, limitations, and future perspectives regarding the method and its application.

2. Method

The model of ocular ambient irradiance is derived through hemispherical harmonic regression (for the direct component) and nonlinear regression (for the diffuse and ground-reflected components) applied to reference data samples. These samples are obtained using the numerical model described in [25]. The validated model requires two inputs to operate: data on the light source (sun position and ambient irradiance values) and a triangular mesh. The triangular mesh approximates a real object with complex geometry by using a significant number of flat triangles. Once the inputs are set, the validated model enables the calculation of the ambient irradiance received by the triangular mesh based on the given ambient irradiance values. This allows us to estimate the distribution of received irradiance, taking into account the geometry of the mesh. The reference samples are therefore computed using a 3D reference model of the human head.

The method used can be summarized in three steps, illustrated in the block diagram shown in Fig. 1: (1) configuration, where we analyzed the problem and define the necessary reference systems; (2) dataset creation, where we used a representative head model as triangular mesh to generate the reference datasets using the validated model described in [25]; and (3) fitting, where we analyzed the datasets and selected and applied the most appropriate regression models.

The use of the validated model for generating reference datasets has two primary advantages. First, being validated, it does not necessitate the validation of the derived analytical model. The corresponding uncertainties will be considered in the regression and 'absorbed' within the confidence interval expressed by the regression parameters. Second, this validated model allows us to simulate data which has proven quite difficult to measure in reality [16]. Furthermore, the intrinsic difficulty in controlling the corresponding light source–due to its variability and complexity–would result in a measurement process with many degrees of freedom.

Utilizing regression models to fit the reference dataset allows us to synthesize the results obtained from the numerical model by explicitly expressing the key variables of the problem, namely sun position, head orientation, and source intensity.

The analytical model is derived by considering the three distinct components that constitute the global irradiance (I_{glo}): direct irradiance (I_{dir}), diffuse irradiance (I_{dif}), and ground-reflected irradiance (I_{ref}). The global ocular irradiance received by the eye is defined as the sum of these components:

$$I_{glo} = I_{dir} + I_{dif} + I_{ref} \tag{1}$$

Furthermore, if the irradiance as a function of time t is known, it is then possible to derive the exposure, expressed in terms of radiant exposure H, as:

$$H(t - t_0) = \int_{t_0}^{t} I(\tau) d\tau \tag{2}$$

where I is a generic irradiance, which can coincide with the global irradiance or one of its three components or combinations, while $t - t_0$ is the time interval of the exposure.

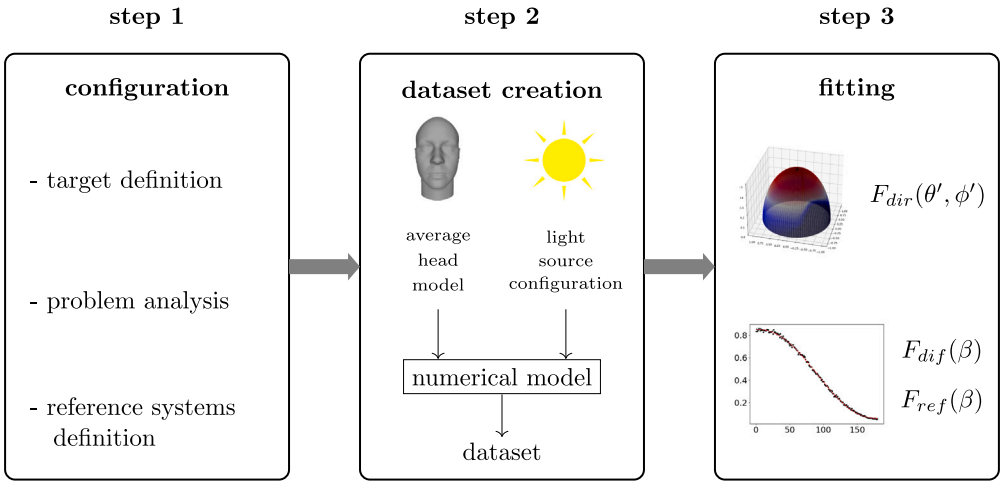

Fig. 1. Block diagram illustrating the method used. In step 1, we defined the target, then analyzed and established the reference systems. In step 2, we used the numerical model described in [25], setting the light source and utilizing the representative triangular mesh as input to obtain the reference dataset. In step 3, we defined regression models and derived parameters by applying them to fit the reference data.

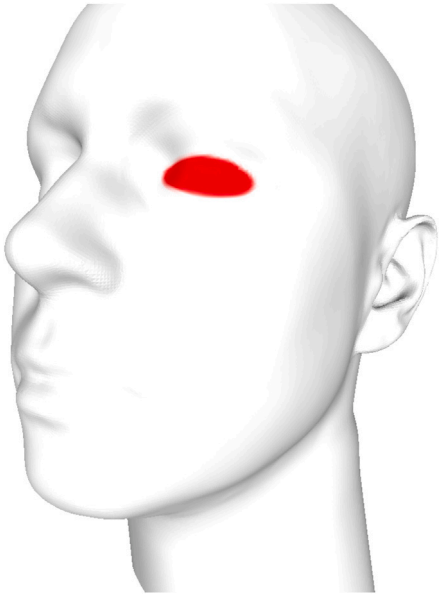

Fig. 2. The head model used in this study with the ocular zone serving as the reference area for ocular irradiance calculations (red area).

2.1. The head model

The distinct facial characteristics and morphological diversity of the human head lead to variations in the ocular irradiance model. To establish a generalized model, an average head must be used. Our goal was to determine a model of ocular irradiance that is representative of an average population.

The U.S. National Institute for Occupational Safety and Health (NIOSH) has created some reference headforms by averaging the 3D scans of approximately 1000 individuals [26], effectively representing the variation within the global population [27]. Among the available headforms (medium, small, and large sizes), the medium-sized headform is the reference for this study. The head model consists of a total of 156 000 vertices and 306 000 faces.

The target area, defined as the sensitive area for ocular irradiance calculations, was selected as mentioned in [27] (considering the reference data on inner and outer canthal distance, and interpupillary distance), and is depicted in Fig. 2. Since the head model represents an average individual, its level of detail is limited. Consequently, the ocular irradiance referred to in this study is the irradiance received by an average ocular area, roughly encompassing the cornea, sclera, and eyelids.

2.2. Reference systems

Two different reference systems are considered for defining the ocular irradiance model: the horizontal reference system and the head reference system.

The horizontal reference system, denoted as O, is fixed to the observer at a specific point on the earth's surface. The set of axes forming its base consists of the x-axis, oriented towards the east (E), the y-axis, oriented towards the north (N), and the z-axis, oriented towards the zenith (Z). In this reference system, the position of the sun, represented by the vector $\mathbf{s}$, is described by the solar zenith angle (θ), the angle between the z-axis and $\mathbf{s}$, and the solar azimuth angle (ϕ), the angle between the y-axis and the projection of $\mathbf{s}$ onto the xy-plane (horizontal plane), positive for clockwise rotations respect to the y-axis.

The head reference system, denoted as O', is fixed to the head. The set of axes forming its base is oriented in such a way that the x'-axis lies at the intersection of the frontal and transverse planes of the head. The direction of x' is determined by the vector "emerging" from the right ear. The y'-axis lies at the intersection of the frontal and sagittal planes. The direction is determined by the vector "emerging" and moving towards the feet. The z'-axis lies in the transverse plane and parallel to the optical axis. The direction is determined by the vector "emerging" frontally.

Since this is an irradiance model, defining the center of the O' system is irrelevant. It can be regarded as a reference system for either the head or the eye. In O', θ' and ϕ' are defined in the same way as θ and ϕ in O.

The head can carry out various rotations: in general, these can occur around each axis. However, to reduce the degrees of freedom and consequently the complexity of the model, we impose that the head can only perform rotations around the x'-axis (pitch) and rotations around the y'-axis (yaw/heading). Furthermore, rotations around the x'-axis are limited to values within the range [0, 180°], where 0° corresponds to the head oriented towards the zenith and 180° corresponds to the head oriented towards the nadir. The decision not to consider rotations around the z'-axis (roll) is supported by the fact that this type of rotation is not frequently performed [28]. The limitation on rotations with respect to the x-axis is based on the same assumption. To describe these rotations, we align the centers of the two reference systems and define the angle β as the angle between Z and z', and the angle α as the angle between N and the intersection between the plane $y'z'$ and the horizontal plane.

The two reference systems and the described variables are illustrated in Fig. 3.

2.3. Direct component

The direct ocular irradiance can be expressed as a fraction of the direct solar irradiance that illuminates the ocular area from an arbitrary direction. This percentage value varies based on the relative position of the sun and the orientation of the head. We define the fraction of direct irradiance as the following quantity:

$$F_{dir} = \frac{I_{dir}}{\mathrm{DNI}} \tag{3}$$

where DNI represents the direct normal irradiance. The function F_{dir} is defined over the domain specified by the set of directions the sun can assume. In the O' system, this means that $\theta' \in [0, \pi]$ and $\phi' \in [0, 2\pi)$. However, for a substantial portion of this domain, $F_{dir} = 0$ because the sun illuminates the head from posterior positions, and therefore cannot directly illuminate the ocular area. The only exception lies in the directions where the eye can be illuminated from one side. In this case, the eye can receive light up to 100° from the optical axis [29]. Since this is a relatively small value, and it contributes modestly to ocular irradiance, we restrict the entire domain of possible sun directions to the frontal hemisphere, that is, $\theta' \in [0, \pi/2]$.

On this domain, the hemispherical harmonics (HH) are defined. In general, we can express our F_{dir} expanded as a series of HH as follows:

$$F_{dir} = \sum_{l=0}^{\infty} \sum_{m=-l}^{l} a_l^m H_l^m(\theta', \phi') \tag{4}$$

where a_l^m are the coefficients of the harmonics of degree l and order m, where $l, m \in \mathbb{N}$ and $|m| \leq l$. The scope is to find the degree L for which the following approximation can be written:

$$F_{dir} \approx \sum_{l=0}^{L} \sum_{m=-l}^{l} a_l^m H_l^m(\theta', \phi') \tag{5}$$

For this study, we used the HH described in [30]. To derive the F_{dir}, we simply set DNI = 1 and computed I_{dir} for various sun directions in O'. Subsequently, the coefficients a_l^m are obtained through the least squares method, using the Moore–Penrose pseudo-inverse as in previous studies [31].

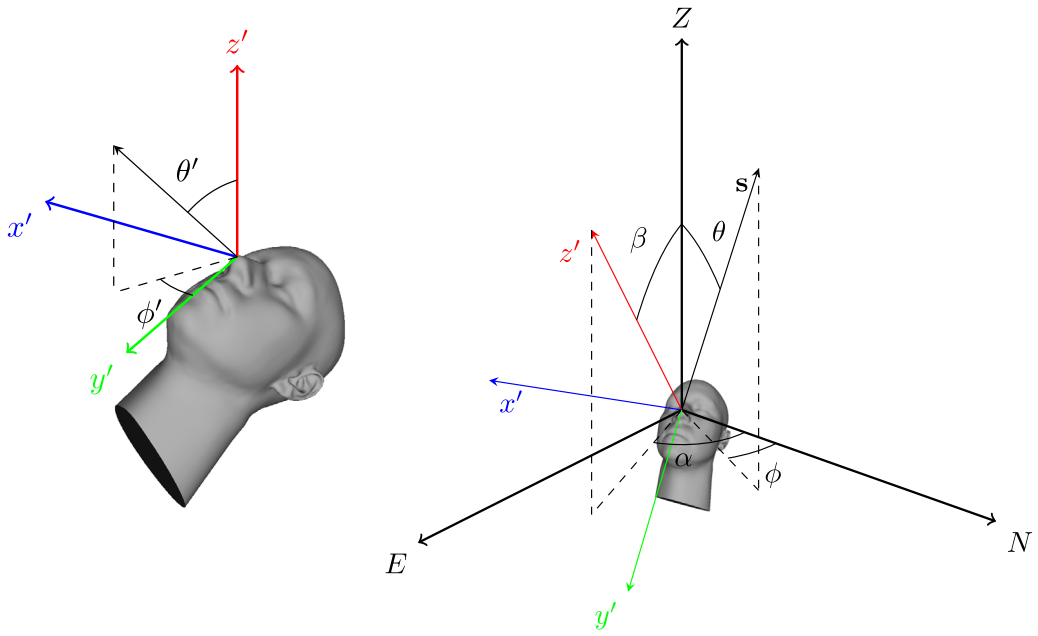

Fig. 3. THe head reference system O' (left), and the horizontal reference system O (right) in which the relative position of the sun **s** and the orientation of the head reference system are described.

Once the function F_{dir} is derived, it is possible to calculate I_{dir} given the head's orientation angles expressed in O (β and α). A rotation of the HH can be defined as previously with spherical harmonics [32]. However, we find it more convenient express θ' and ϕ' through a simple change of basis:

$$\begin{aligned}\theta' &= \arccos[\sin\theta\sin\beta\cos(\phi-\alpha)+\cos\theta\cos\beta]\\ \phi' &= \text{atan2}[-\sin\theta\cos\beta\cos(\phi-\alpha)-\cos\theta\sin\beta, \sin\theta\sin(\phi-\alpha)]\end{aligned} \tag{6}$$

2.4. Diffuse and reflected component

The sources of diffuse and ground-reflected irradiance are simplified to isotropic sources. Consequently, the fraction of the diffuse and ground-reflected irradiance received depends only on the position of the horizon relative to the head. For a given position, the fraction of diffuse irradiance corresponds to the fraction of the sky visible from the target surface. This fraction is also known as the radiation view factor [33]. We define the fraction of diffuse irradiance as follows:

$$F_{dif} = \frac{1}{\pi A_o}\int_{A_o}\int_{\Omega_{vis}} \cos\gamma \, dA \, d\Omega \tag{7}$$

where A_o is the ocular area on which the irradiance is calculated, γ is the angle between the normal vector at an arbitrary point on the surface A_o and the unit vector that, from the arbitrary point, is oriented towards $d\Omega$, and Ω_{vis} is the solid angle of the visible sky. Using isotropic sources introduces symmetry with respect to rotations around the vertical axis. Consequently, the variable α can be removed. It follows that $F_{dif} = F_{dif}(\beta)$. The calculation of the fraction of ground-reflected irradiance F_{ref} is performed in the same way, but using Ω_{vis} as the solid angle of visible ground and integrating over the lower hemisphere. For details, refer to [25].

To obtain the data for fitting, it is necessary to calculate Eq. (7) for various values of β. Our initial results exhibit a trend similar to that of a cosine function [34]. However, a function that proves to be particularly suitable for fitting is a composition of a sigmoid function and a linear function. The functions F_{dif} and F_{ref} exhibit identical trends because their sum represents the radiation view factor for the entire ocular region, which remains constant. Consequently, the same parameters can be used for both functions, with a simple geometric reflection applied with respect to the axis corresponding to the intersection of the two functions, which occurs at $\beta = \pi/2$. The final function used for the fit is the following four-parameter function:

$$F_{dif}(\beta) = a(\beta - \frac{\pi}{2}) + \frac{b}{1+e^{c(\beta-\frac{\pi}{2})}} + d \tag{8}$$

where β is in radiant, and a, b, c, and d are the parameters to be determined through regression. The model for the ground-reflected component is therefore derived by manipulating the last equation:

$$F_{ref}(\beta) = -a(\beta - \frac{\pi}{2}) + \frac{b}{1+e^{-c(\beta-\frac{\pi}{2})}} + d \tag{9}$$

2.5. The model

The final model for ocular irradiance, incorporating all the described variables and considering the symmetry between the right and left ocular regions, can be written as follows:

$$I_{glo} = F_{dir}(\theta', p\phi')\,\text{DNI} + \left[F_{dif}(\beta) + \rho\, F_{ref}(\beta)\right]\text{DHI} \tag{10}$$

where θ' and ϕ' are calculated from θ, ϕ, β and α according to the formulas (6), while p is the eye side, defined as:

$$p = \begin{cases} 1 & \text{for left eye} \\ -1 & \text{for right eye} \end{cases} \tag{11}$$

The ocular irradiance model can finally be integrated into Eq. (2) through numerical implementation. This allows for obtaining the radiant exposure value resulting from an exposure of a known duration. In this case, the more general version of the model involves the use of time-dependent DNI and DHI, as well as head orientation. The albedo ρ can also be time-dependent, describing the individual's potential spatial variation relative to the ground during the exposure period.

The model is based on radiometric quantities (irradiance and radiant exposure), but naturally, it can be used with photometric variables (illuminance and luminous exposure) using the appropriate conversion.

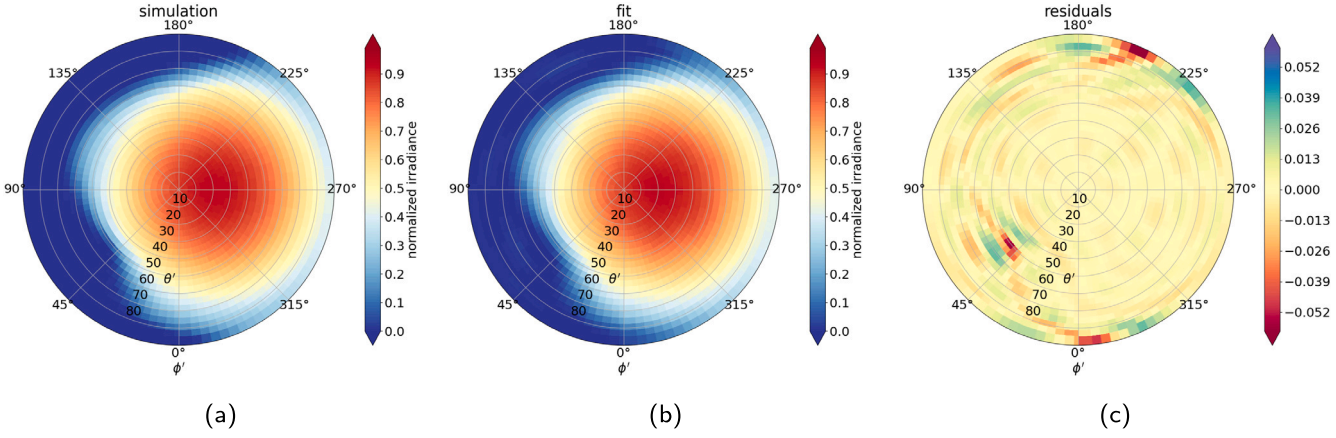

Fig. 4. The nearest interpolation of the dataset obtained through numerical simulations and HH regression in polar coordinates (the zenith angle θ' corresponds to the radial variable, while the azimuthal angle ϕ' corresponds to the angular variable). Figure (a): F_{dir} calculated through numerical simulation using the *in silico* reference head model and the ocular region as the target surface for a total of 2500 points. Figure (b): result of HH regression applied to F_{dir} with degree $L = 9$. Figure (c): residuals obtained by the difference between F_{dir} and the regression.

3. Results

3.1. Direct component

The function F_{dir} was derived using 2500 equidistant points in the defined domain. The aim was to find the lowest number of parameters a_l^m that can satisfactorily fit the data. To evaluate the regression we calculated the root-mean-square-error (RMSE), analyzed the residuals plots, and applied the multivariate Kolmogorov–Smirnov test [35].

The RMSE decreases with increasing degree L and converges to values on the order of 10^{-5} starting from $L = 14$. For each specific degree, we analyzed the residual plot around L to determine the quality of the regression. It is noted that some areas of the domain are a bit more challenging to fit. In particular, this occurs in some areas of the graph where a strong gradient appears, such as at $\theta' = 90°$ and $\phi' = 0°$. The area around the nose exhibits a similar trend, which disappears completely for higher L degrees. The same applies to marginal values at $\theta' = 90°$ and $\phi' = 200°$. These areas always correspond to a strong gradient of F_{dir}.

The plot of the function F_{dir}, depicted in Fig. 4-a, resemble a cosine function of revolution near to $\theta' = 0°$. However, as we deviate from this value, the function decreases more rapidly than a cosine towards the nasal area, while remaining constant towards the opposite side up to about 50°. The flattening of the function due to head anatomy is quite noticeable. The boundary region that starts around $\phi' = 0°$ (due to the cheek) and continues all the way to approximately $\phi' = 225°$ clockwise is the effect of shading caused by the nose and forehead. The nose is particularly prominent, extending for an interval of about 90°. The spatial extension of the nose results in the function F_{dir} being nearly zero for an interval of azimuth angle of about $\phi' = 40°$.

We found that a good compromise between the number of regression coefficients and the quality of the fit starts from $L = 9$, for a total of 100 coefficients. In Fig. 4-b, the fit obtained using HH with degree $L = 9$ is plotted. For this degree value, the differences observed in the mentioned areas never exceed 8% of the percentage difference compared to the reference. Furthermore, this difference is observed for a limited number of points considering the entire available dataset. The largest differences are found where F_{dir} transitions from a very low value (close to zero) to a typically higher value of 0.3 or more.

Fig. 4-c shows the residuals obtained between the reference dataset and the regression. The distribution is uniform around zero (standard error of residuals of $1.6 \cdot 10^{-2}$), except for the points just discussed. A multivariate Kolmogorov–Smirnov test [35] showed a p-value of 0.6, confirming the goodness of fit.

In the fit obtained using degree $L = 9$, there are some regions in the domain where F_{dir} is negative. However, all of these regions are within the shadow zone highlighted in Fig. 4-a. Furthermore, the lowest values do not go below -0.03. Naturally, this trend is reduced as L increases. These values are retained for subsequent analyses. For the final calculation of I_{dir}, they can be easily filtered and replaced with null values without losing any information.

The difficulties in fitting the data in some areas where a gradient of F_{dir} is shown may result from how the dataset was computed. The head model, in fact, consists of flat triangles. The shadow that is cast on the target surface therefore reduces its extent abruptly between one data point and another. Although this aspect can be reduced by increasing the total number of points, it cannot be completely eliminated.

3.2. Diffuse and reflected component

To obtain a single data point for the entire reference dataset, we took the average of eight different simulations keeping the same value of β. Each simulation was obtained by using 10^4 points of integration (random) for each triangle of the target domain. The number of data points used for the fit is 180, and the domain were subdivided homogeneously.

The reference dataset obtained through simulations and the fit obtained using Eq. (8) as the regression model are depicted in Fig. 5. The fit proves to be suitable for describing the distribution of the obtained data ($R^2 = 0.999$, adj-$R^2 = 0.994$, and RMSE $= 10^{-5}$). Hypothesis tests applied to the parameters obtained from the linear regression of observed vs. predicted data [36] have positive results at the 5% significance level.

The residual plot reveals linearity between the model and the data, with the exception of angles within the interval $[150°, 180°]$. In this interval, the linearity relationship is not preserved, although the values are evenly distributed around zero on average. In this range, the calculated values never exceed the standard error of the residuals (the maximum value they reach is ± 0.011). Additionally, when calculating studentized residuals, no outliers are observed. Therefore, due to its limited magnitude we do not consider that this variation, although it may potentially be reduced with a more complex regression model, affects the goodness of fit of the model in describing our dataset. The values of the four regression parameters, along with the corresponding 95% of confidence interval, are reported in Table 1.

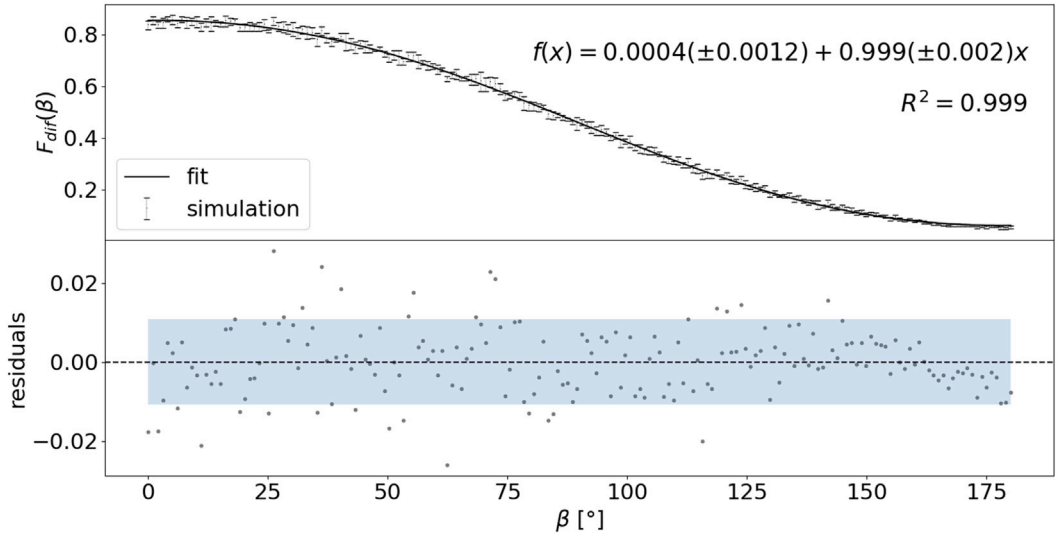

Fig. 5. Diffuse fraction of irradiance ($F_{dir}(\beta)$) for different head angles. The points represent the simulated data, while the line represents the fit. Uncertainty corresponds to the standard deviation of the eight different simulations for each point. The function $f(x) = a + bx$ is the model of linear regression (within parentheses, the standard error of the mean) used to fit observed versu predicted data with the corresponding correlation coefficient. In the lower part, the residuals are plotted, with the shaded region indicating the standard error of the residuals.

Table 1
Values of the regression parameters obtained using the model expressed by Eq. (8) and their respective 95% confidence intervals.

Parameter	Value	CI (95%)
a	0.384	[0.098, 0.670]
b	2.713	[1.057, 4.369]
c	1.201	[0.991, 1.411]
d	−0.899	[−1.282, −0.516]

3.3. Example of output

In this section, we present an illustrative example of utilizing the described model, drawing inspiration from various publications involving measurement campaigns using manikins [16]. In these studies, light sensors were positioned in the eye socket of a manikin, which was then exposed to sunlight.

The manikins are typically placed upright (i.e., $\beta = 90°$) and rotated to always face the sun (i.e. $\alpha = \phi$). From these studies, the emergence of a bimodal function is well-known. The measured irradiance on the ocular area increases as the solar zenith angle decreases. Beyond a certain value, the head's anatomy prevents the sun from directly illuminating the eye. As a result, in warmer months, the eye records a lower value of direct irradiance during the maximum daily level of ambient irradiance.

To replicate a similar trend, we acquire the necessary data for the simulation using the radiative transfer model LibRadtran [37]. We considered a latitude of 30° and generate the DNI using a typical atmospheric profile for these latitudes, limited to the UVB range (280–315 nm) and cloudiness. With the intention of observing how ocular irradiance changes across different months of the year, we generated **s** for a day of each month in the year 2023 (precisely, the 22nd of each month). The angles θ and ϕ, along with DNI, are generated for each of these days over a 24-h period with a time step of 5 min. The results are depicted in Fig. 6.

In this figure, we observe the distinct trends of the received direct ocular irradiance for each month. Except for the two solstices in June and December, the results cluster in pairs of months due to the quasi-symmetrical behavior in the apparent solar time throughout the year. It is evident that starting from December (the month when the maximum daily sun elevation is the lowest of the year, approximately 37 degrees, which is the co-latitude minus the earth's axial tilt angle, the direct ocular irradiance increases. The intensity is recorded over an increasingly extended time period due to the lengthening of the days between the two solstices. Until February/October, the intensity increase is gradual, and the pattern remains similar, peaking at local noon ($\phi = 180°$). However, as we approach the equinoxes, the function starts to flatten, and two distinct peaks begin to form. This characteristic is due to the head's anatomy and the chosen latitude for generating the results. The bimodal distribution with its two peaks becomes more pronounced as we approach the summer solstice. The intensity recorded at local noon tends to decrease, while the maximum intensity does not increase but rather shifts to occur earlier in the morning or later in the evening.

Direct comparisons with the findings highlighted by measurements conducted using manikins are not feasible since the result depends on the manikin head's anatomy and the defined target area used as a reference for measurement. However, we can observe trends similar to the ones observed in the manikin experiments: the formation of the bimodal function and the gradual decrease in ocular irradiance at local noon as the solar zenith angle decreases [16].

4. Discussion

In this study, we presented the derivation of a model for ocular ambient irradiance. This model was developed by applying specific regression techniques to reference data, which were derived from a validated numerical model capable of simulating ocular irradiance.

The use of the validated numerical model enabled us to estimate the ambient irradiance received specifically by the ocular region by generalizing the orientation of the head. With this approach, we were able to estimate a quantity that would be challenging to obtain in reality, especially while maintaining the same degrees of freedom.

The application of regression models aims to synthesize the reference data obtained from the validated numerical model, thereby creating a simplified model of ocular irradiance composed of measurable and estimable variables (head rotation, sun position, and radiation intensity).

The chosen regression models are (1) expansion in hemispherical harmonics for the direct component and (2) a combination of a linear model and a sigmoid function for the diffuse and ground-reflected components. The total number of parameters used to fit the direct

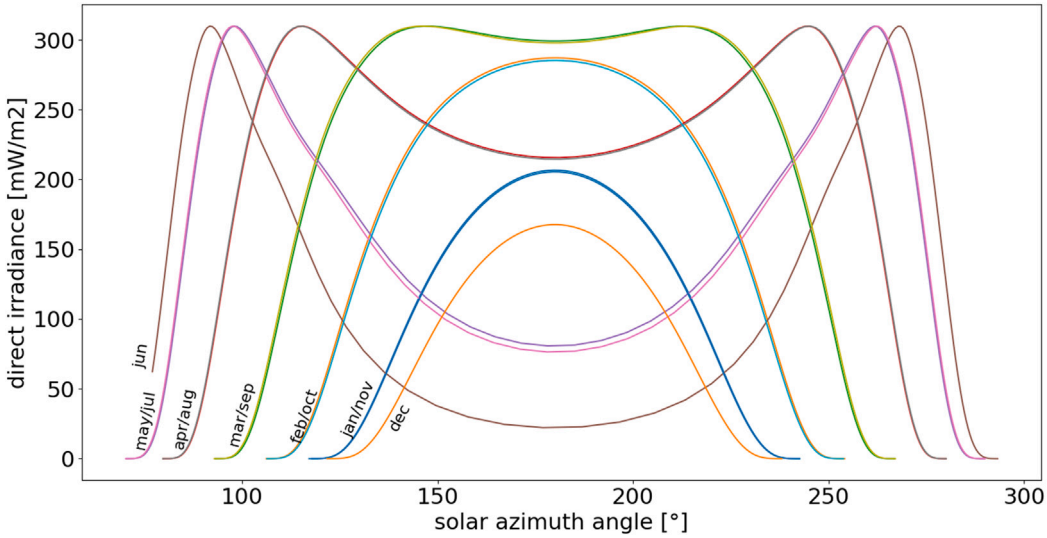

Fig. 6. Output obtained from the model presented in this study, using θ and ϕ at a point on the Earth's surface at 30° latitude on the 22nd of each month. The head is oriented so that $\beta = 90°$ and always faces the sun ($\alpha = \phi$).

component is 100 ($L = 9$), while four parameters are used for the remaining components.

The analyses show an excellent level of agreement between the fits and the datasets. The chosen regression models accurately describe the trends observed in the datasets. Goodness-of-fit tests for the direct component ensure that the chosen degree (e.g., L) can describe the dataset. Analysis of residuals and RMSE confirm this. The t-tests performed on the parameters of the linear regression obtained from the simulation-fit relation for the diffuse and ground-reflected components show a statistically significant relationship.

The model serves as a fast and cost-effective method for determining the fraction of irradiance received by the eye in an outdoor light exposure scenario. It allows for the calculation of this quantity for different head orientations, taking into consideration the influence of anatomy, which inherently affects the distribution of received irradiance as the head orientation changes.

This model can be employed as a research tool to investigate the relationship between ambient irradiance and ocular irradiance in various scenarios. Ideally, it can find application in research areas where the calculation or prediction of ocular irradiance is taken into consideration.

The fraction of diffuse irradiance, F_{dif}, can be used to obtain a more accurate estimate of ocular diffuse irradiance compared to the simple Liu–Jordan model [34], which is often used for this purpose, although it refers to an non-obstructing surface. In this case, the model provides a correction term to ascertain diffuse ocular exposure.

The model could be used in conjunction with experimental measurements to assess ocular exposure (or over an extended period) for a specific individual or a group of individuals in particular locations and for specific tasks. To achieve this, it would be necessary to measure DNI and DHI, or simulate with a radiative transfer model (such as the aforementioned LibRadtran [37] or any other radiative transfer model, like SMARTS [38]), and calculate the sun's position using specific algorithms (such as the one proposed in [39], depending on the desired level of accuracy). To measure head orientation, various methodologies and measurement tools could be used, such as miniaturized accelerometers [19,40], wearable sensors [41] or, more generally, complex systems like motion capture systems [42].

We posit that this model also could be used in the study of certain ocular pathologies induced by ambient UVR. For instance, it is know that pterygium has a higher incidence in the terrestrial belt between 40 degrees north and 40 degrees south, a correlation that associates this pathology with ambient UVR [43]. However, concrete estimates of exposure are currently lacking.

The model could be used to study the relationship between ocular dose and latitude [44]. Similarly, it can be employed to investigate the relationship between ocular dose and the seasonal variability of a particular location [45].

The same concept can be applied to the investigation of the relationship between time spent outdoors and the onset of myopia. With this model, it would be possible to estimate ocular dose and study the relationship between the onset of myopia and the ocular dose, rather than the time spent outdoors [46].

By iterating the model, it is possible to obtain simulations that vary with ambient parameters and different head orientations. In this manner, ocular irradiance can be predicted for long-term exposures, where measurements are typically limited and challenging to perform.

In this regard, the model could be applied to determine how ocular irradiance will vary in scenarios of climate change. There is indeed an expected increase in ambient UVR [23,24], which will result in a subsequent increase in ocular exposure. By understanding how ambient irradiance will change in the coming decades, it is possible to use the model presented in this work to determine the consequent impact on ocular irradiance.

4.1. Limitations and future perspectives

This model was developed as a method of establishing a relationship between ambient irradiance and ocular irradiance. During the derivation process, it was necessary to make approximations and simplifications, which naturally introduce limitations to the model's application and its ability to determine the desired quantity. Depending on its applications and usage, the model can be further improved and modified for future specific applications.

The choice to approximate the diffuse and ground-reflected light component with isotropic sources significantly simplifies the model. However, in some situations, it may introduce some discrepancies when compared to real-world data, as widely reported in other studies [47,48]. Nevertheless, several models of anisotropic diffuse irradiance are derived from the isotropic model [49]. Integrating these adaptations into the current model could enhance the accuracy of determining the diffuse and reflected components, albeit at the cost of increased complexity.

A more faithful implementation would require the integration of sky radiance. However, in the vast majority of measurements, DNI and

DHI are obtained. Models of sky radiance exist (for instance, the model proposed in [50]), but since our model is derived from regression, it is not feasible to synthesize the wide variability of radiance distribution in the sky into a single simple model.

As previously mentioned, the model presented in this study is based on datasets obtained by referring to the ocular region (the red area in Fig. 2). This region is relatively extensive and includes the cornea, sclera, and the edges of the eyelids. This constraint arises from the head model we used, which lacks detailed representation of the ocular region, as it is an average surface. Thus, the model does not differentiate the irradiance received from individual ocular components; instead, it describes the average irradiance received by the entire ocular region. A more targeted model focusing on specific components would be beneficial for certain applications. For instance, a corneal irradiance model would be particularly useful for studying the relationship between ambient UV exposure and the development of cataracts. Alternatively, a model specifically focused on the eyelids would allow for a targeted investigation into the relationship between ambient UVR and eyelid tumors [51].

To develop a specific model for each ocular component, it would be necessary to implement an anatomical eye model on a reference mesh, as in [52]. In this case, it would be possible to define irradiance fractions F_{dir}, F_{dif}, F_{ref} specific to the cornea, sclera, and eyelids by building an analytical model for each specific component. With reference datasets available for each component, it might be possible to create a unified regression model where each component is specified by a particular set of parameters.

However, due to the increased complexity of the reference area, the number of parameters required for the hemispherical harmonics expansion might need to be further increased to effectively describe the results. Similarly, the regression model used for the diffuse and reflected irradiance components would need to be modified to accurately capture the variability of the required quantities.

It would be possible to increase the degrees of freedom of the model and include the orientation of the eye as well. Formally, this modification would require the combination of two hemispherical harmonics for the direct component of ambient irradiance and the modification of the regression model (likely with the addition of further parameters) for the remaining components. This derivation would allow for understanding the variability of the received ocular dose for different viewing angles. Furthermore, the relationship presented in [53] that links ambient luminance with the aperture angle of the eyelid could be implemented.

Ideally, by associating the numerical model used to generate the fitted datasets with an eye model [54], the same method could be implemented to derive an analytical model of the average dose received by ocular tissues.

The model, written in the Python programming language, has already been implemented and can be downloaded along with the HH regression parameters at the following link: https://github.com/mm-89/OcularAmbientIrradianceModel.

Funding

This research was developed within the framework of the InExES project: Coupling Internal and External Eye Simulation for a Better Prediction of Natural and Artificial Light Exposure (Internal and External Eye Simulation) which is financially supported by the Velux Stiftung in Zürich, Switzerland (Grant number 1254).

CRediT authorship contribution statement

Michele Marro: Conceptualization, Visualization, Validation, Resources, Methodology, Investigation, Formal analysis, Data curation, Figures, Writing. **Laurent Moccozet:** Final editing, Funding acquisition. **David Vernez:** Review & editing.

Declaration of competing interest

The authors declare that they have no known competing financial interests or personal relationships that could have appeared to influence the work reported in this paper.

References

[1] J. Yam, A. Kwok, Ultraviolet light and ocular diseases, Int. Ophthalmol. 34 (2014) 383–400.
[2] R.E. Reale, R.M. Lucas, S.N. Byrne, L. Hollestein, L.E. Rhodes, S. Yazar, A.R. Young, M. Berwick, R.A. Ireland, C.M. Olsen, The effects of exposure to solar radiation on human health, Photochem. Photobiol. Sci. 22 (5) (2023) 305–318.
[3] M.J. Ang, N.A. Afshari, Cataract and systemic disease: A review, Clin. Exp. Ophthalmol. 49 (2) (2021) 118–127, arXiv:https://onlinelibrary.wiley.com/doi/pdf/10.1111/ceo.13892. [Online]. Available: https://onlinelibrary.wiley.com/doi/abs/10.1111/ceo.13892.
[4] C. Lee, N. Afshari, The global state of cataract blindness, Curr. Opin. Ophthalmol. 28 (2016).
[5] J. Moan, M. Grigalavicius, Z. Baturaite, A. Dahlback, A. Juzeniene, The relationship between UV exposure and incidence of skin cancer, Photodermatol. Photoimmunol. Photomed. 31 (1) (2015) 26–35, arXiv:https://onlinelibrary.wiley.com/doi/pdf/10.1111/phpp.12139. [Online]. Available: https://onlinelibrary.wiley.com/doi/abs/10.1111/phpp.12139.
[6] W.-P. Zhou, Y.-F. Zhu, B. Zhang, W.-Y. Qiu, Y.-F. Yao, The role of ultraviolet radiation in the pathogenesis of pterygia (review), Mol. Med. Rep. 14 (2016).
[7] W. Chu, H. Choi, A. Bhat, V. Jhanji, Pterygium: new insights, Eye 34 (2020).
[8] A.R. Muralidharan, C. Lança, S. Biswas, V.A. Barathi, L.W.Y. Shermaine, S. Seang-Mei, D. Milea, R.P. Najjar, Light and myopia: from epidemiological studies to neurobiological mechanisms, Ther. Adv. Ophthalmol. 13 (2021) 25158414211059246, arXiv:https://doi.org/10.1177/25158414211059246. [Online]. Available: https://doi.org/10.1177/25158414211059246. PMID: 34988370.
[9] B.L. Diffey, Sources and measurement of ultraviolet radiation, Methods 28 (1) (2002) 4–13, [Online]. Available: https://www.sciencedirect.com/science/article/pii/S1046202302002049.
[10] L. Wald, Fundamentals of Solar Radiation, 2021.
[11] J. Sun, R. Lucas, S. Harrison, I. van der Mei, B. Armstrong, M. Nowak, A. Brodie, M. Kimlin, The relationship between ambient ultraviolet radiation (UVR) and objectively measured personal UVR exposure dose is modified by season and latitude, Photochem. Photobiol. Sci. 13 (2014).
[12] M.-A. Serrano, J. Cañada, J. Moreno, G. Gurrea, Personal UV exposure for different outdoor sports, Photochem. Photobiol. Sci.: Off. J. Eur. Photochem. Assoc. Eur. Soc. Photobiol. 13 (2014).
[13] B.L. Diffey, Time and place as modifiers of personal UV exposure, Int. J. Environ. Res. Public Health 15 (6) (2018) [Online]. Available: https://www.mdpi.com/1660-4601/15/6/1112.
[14] D.H. Sliney, How light reaches the eye and its components, Int. J. Toxicol. 21 (6) (2002) 501–509, [Online]. Available: https://doi.org/10.1080/10915810290169927. PMID: 12537646.
[15] G. Ziegelberger, ICNIRP guidelines on limits of exposure to incoherent visible and infrared radiation, Health Phys. 105 (2013) 74–96.
[16] M. Marro, L. Moccozet, D. Vernez, Assessing human eye exposure to UV light: A narrative review, Front. Public Health 10 (2022) [Online]. Available: https://www.frontiersin.org/articles/10.3389/fpubh.2022.900979.
[17] N. Hatsusaka, Y. Seki, N. Mita, Y. Ukai, H. Miyashita, E. Kubo, D.H. Sliney, H. Sasaki, UV index does not predict ocular ultraviolet exposure, Transl. Vis. Sci. Technol. 10 (2021).
[18] M. Moehrle, B. Dennenmoser, C. Garbe, Continuous long-term monitoring of UV radiation in professional mountain guides reveals extremely high exposure, Int. J. Cancer J. Int. Cancer 103 (2003) 775–778.
[19] J. Stampfli, B. Schrader, C. Battista, R. Haefliger, O. Schälli, G. Wichmann, C. Zumbühl, P. Blattner, C. Cajochen, R. Lazar, M. Spitschan, The light-dosimeter: A new device to help advance research on the non-visual responses to light, Light. Res. Technol. 55 (2023) 147715352211471.
[20] X. Huang, A. Chalmers, Review of wearable and portable sensors for monitoring personal solar UV exposure, Ann. Biomed. Eng. 49 (2021).
[21] M.M. Sydenham, M.J. Collins, L.W. Hirst, Measurement of ultraviolet radiation at the surface of the eye, Invest. Ophthalmol. Vis. Sci. 38 (8) (1997) 1485–1492, arXiv:https://arvojournals.org/arvo/content_public/journal/iovs/933424/1485.pdf.
[22] J.-i. Kim, J.-d. Cho, J. Son, C.H. Choi, H.G. Wu, J.M. Park, Contact lens-type ocular in vivo dosimeter for radiotherapy, Med. Phys. 47 (2019).
[23] P. Barnes, C. Williamson, R. Lucas, S. Robinson, S. Madronich, N. Paul, J. Bornman, A. Bais, B. Sulzberger, S. Wilson, A. Andrady, R. McKenzie, P. Neale, A. Austin, G. Bernhard, K. Solomon, P. Young, M. Norval, R. Zepp, Ozone depletion, ultraviolet radiation, climate change and prospects for a sustainable future, Nat. Sustain. 2 (2019).

[24] C. Baldermann, G. Laschewski, J.U. Grooß, Impact of climate change on non-communicable diseases caused by altered UV radiation, J. Health Monit. 8 (Suppl 4) (2023) 57–75, [Online]. Available: https://pubmed.ncbi.nlm.nih.gov/37799535/.

[25] M. Marro, L. Moccozet, D. Vernez, A numerical model for quantifying exposure to natural and artificial light in human health research, Comput. Biol. Med. (2024) 108119, [Online]. Available: https://www.sciencedirect.com/science/article/pii/S0010482524002038.

[26] NIOSH, Anthropometric data and ISO digital headforms, 2003, [Online]. Available: https://www.cdc.gov/niosh/data/datasets/rd-10130-2020-0/default.html.

[27] G. Niezgoda, Z. Zhuang, Development of headforms for ISO eye and face protection standards, Procedia Manuf. 3 (2015) 5761–5768.

[28] S. Willemsen, L. Oostwoud Wijdenes, R. Beers, M. Koppen, P. Medendorp, Natural statistics of head roll: implications for Bayesian inference in spatial orientation, J. Neurophysiol. 128 (2022).

[29] H.K. Walker, W.D. Hall, J.W. Hurst, Clinical Methods, in: The History, Physical, and Laboratory Examinations, Butterworths, 1990.

[30] P. Gautron, J. Krivanek, S. Pattanaik, K. Bouatouch, A novel hemispherical basis for accurate and efficient rendering, in: ACM SIGGRAPH 2007 Papers - International Conference on Computer Graphics and Interactive Techniques, 2004, pp. 321–330.

[31] J. Rahola, F. Belloni, A. Richter, Modelling of radiation patterns using scalar spherical harmonics with vector coefficients, in: 2009 3rd European Conference on Antennas and Propagation, 2009, pp. 3361–3365.

[32] Z. SU, P. Coppens, Rotation of real spherical harmonics, Acta Crystallogr. Sect. A 50 (1994).

[33] M.K. Gupta, K.J. Bumtariya, H. Shukla, P. Patel, Z. Khan, Methods for evaluation of radiation view factor: A review, Mater. Today: Proc. 4 (2, Part A) (2017) 1236–1243, [Online]. Available: https://www.sciencedirect.com/science/article/pii/S2214785317301438. 5th International Conference of Materials Processing and Characterization (ICMPC 2016).

[34] B.Y.H. Liu, R.C. Jordan, The long-term average performance of flat-plate solar-energy collectors, Sol. Energy 7 (1963) 53–74, [Online]. Available: https://api.semanticscholar.org/CorpusID:115763706.

[35] G. Fasano, A.C.T. Franceschini, A multidimensional version of the Kolmogorov–Smirnov test, Mon. Not. R. Astron. Soc. 225 (1987) 155–170, [Online]. Available: https://api.semanticscholar.org/CorpusID:122549681.

[36] G. Pineiro, S. Perelman, J.P. Guerschman, J.M. Paruelo, How to evaluate models: Observed vs. predicted or predicted vs. observed? Ecol. Model. 216 (3) (2008) 316–322, [Online]. Available: https://www.sciencedirect.com/science/article/pii/S0304380008002305.

[37] C. Emde, R. Buras-Schnell, A. Kylling, B. Mayer, J. Gasteiger, U. Hamann, J. Kylling, B. Richter, C. Pause, T. Dowling, L. Bugliaro, The libradtran software package for radiative transfer calculations (version 2.0.1), Geosci. Model Dev. 9 (5) (2016) 1647–1672, [Online]. Available: https://gmd.copernicus.org/articles/9/1647/2016/.

[38] C. Gueymard, Simple model of the atmospheric radiative transfer of sunshine (SMARTS), 2023, https://www.nrel.gov/grid/solar-resource/smarts.html. (Accessed 1 January 2023).

[39] R. Grena, An algorithm for the computation of the solar position, Sol. Energy 82 (5) (2008) 462–470, [Online]. Available: https://www.sciencedirect.com/science/article/pii/S0038092X07002162.

[40] L. Miller, J. Urban, V. Whelan, W. Baxter, S. Tatter, J. Stitzel, An envelope of linear and rotational head motion during everyday activities, Biomech. Model. Mechanobiol. 19 (2020).

[41] S. Ionut-Cristian, D. Dan-Marius, Using inertial sensors to determine head motion—A review, J. Imaging 7 (12) (2021) [Online]. Available: https://www.mdpi.com/2313-433X/7/12/265.

[42] B. Cesqui, R.v. de Langenberg, F. Lacquaniti, A. d'Avella, A novel method for measuring gaze orientation in space in unrestrained head conditions, J. Vis. 13 (8) (2013) 28–28. arXiv:https://arvojournals.org/arvo/content_public/journal/jov/933547/i1534-7362-13-8-28.pdf. [Online]. Available: https://doi.org/10.1167/13.8.28.

[43] L. Liu, J. Wu, J. Geng, Z. Yuan, D. Huang, Geographical prevalence and risk factors for pterygium: a systematic review and meta-analysis, BMJ Open 3 (11) (2013) arXiv:https://bmjopen.bmj.com/content/3/11/e003787.full.pdf. [Online]. Available: https://bmjopen.bmj.com/content/3/11/e003787.

[44] H. Sasaki, Y. Sakamoto, C. Schnider, N. Fujita, N. Hatsusaka, D. Sliney, K. Sasaki, UV-B exposure to the eye depending on solar altitude, Eye Contact Lens 37 (2011) 191–195.

[45] H. Li-Wen, G. Qian, X. Wen-Ying, W. Yang, G. Hui-Zhi, D. Guo-Qing, L. Jing-Hai, L. Yang, Diurnal variations in solar ultraviolet radiation at typical anatomical sites, Biomed. Environ. Sci. 23 (3) (2010) 234–243.

[46] L.S. Eppenberger, V. Sturm, The role of time exposed to outdoor light for myopia prevalence and progression: A literature review, Clin. Ophthalmol. 14 (2020) 1875–1890, arXiv:https://www.tandfonline.com/doi/pdf/10.2147/OPTH.S245192. [Online]. Available: https://www.tandfonline.com/doi/abs/10.2147/OPTH.S245192.

[47] N. Kamphuis, C. Gueymard, M. Holtzapple, A. Duggleby, K. Annamalai, Perspectives on the origin, derivation, meaning, and significance of the isotropic sky model, Sol. Energy 201 (2020) 8–12, [Online]. Available: https://www.sciencedirect.com/science/article/pii/S0038092X20301948.

[48] Z. Li, H. Xing, G. Augenbroe, Criterion based selection of sky diffuse radiation models, Sustainable Cities Soc. 50 (2019) 101692, [Online]. Available: https://www.sciencedirect.com/science/article/pii/S2210670719314817.

[49] A.M. Noorian, I. Moradi, G.A. Kamali, Evaluation of 12 models to estimate hourly diffuse irradiation on inclined surfaces, Renew. Energy 33 (6) (2008) 1406–1412, [Online]. Available: https://www.sciencedirect.com/science/article/pii/S0960148107002509.

[50] N. Igawa, Y. Koga, T. Matsuzawa, H. Nakamura, Models of sky radiance distribution and sky luminance distribution, Sol. Energy 77 (2) (2004) 137–157, [Online]. Available: https://www.sciencedirect.com/science/article/pii/S0038092X04001070.

[51] Y. Sato, S. Takahashi, T. Toshiyasu, H. Tsuji, N. Hanai, A. Homma, Squamous cell carcinoma of the eyelid, Japanese Journal of Clinical Oncology 54 (1) (2023) 4–12, arXiv:https://academic.oup.com/jjco/article-pdf/54/1/4/55123919/hyad127.pdf. [Online]. Available: https://doi.org/10.1093/jjco/hyad127.

[52] M. Marro, L. Moccozet, D. Vernez, Modeling the protective role of human eyelashes against ultraviolet light exposure, Comput. Biol. Med. 141 (2022) 105135, [Online]. Available: https://www.sciencedirect.com/science/article/pii/S001048252100929X.

[53] D.H. Sliney, Geometrical assessment of ocular exposure to environmental UV radiation–implications for ophthalmic epidemiology, J. Epidemiol. 9 (6 Suppl) (1999) S22–32, [Online]. Available: https://api.semanticscholar.org/CorpusID:39730302.

[54] D.A. Atchison, L.N. Thibos, Optical models of the human eye, Clin. Exp. Optom. 99 (2) (2016) 99–106, arXiv:https://doi.org/10.1111/cxo.12352. [Online]. Available: https://doi.org/10.1111/cxo.12352.